Supplementary Information for:

Alloying a Single and a Double Perovskite: A Cu$^{+/2+}$ Mixed-Valence Layered Halide Perovskite with Strong Optical Absorption

Bridget A. Connor,[a] Rebecca W. Smaha,[a,b] Jiayi Li,[a] Aryeh Gold-Parker,[a,c] Alexander J. Heyer,[a] Michael F. Toney,[c,d] Young S. Lee,[b,e] and Hemamala I. Karunadasa*[,a,b]

[a] Department of Chemistry, Stanford University, Stanford, California 94305, United States
[b] Stanford Institute for Materials and Energy Sciences, SLAC National Accelerator Laboratory, Menlo Park, California 94025, United States
[c] Stanford Synchrotron Radiation Lightsource, SLAC National Accelerator Laboratory, Menlo Park, California 94025, United States
[d] Department of Chemical and Biological Engineering, University of Colorado Boulder, Boulder, CO 80309, United States
[e] Department of Applied Physics, Stanford University, Stanford, California 94305, United States

*hemamala@stanford.edu

Table of Contents:

S1 Experimental Methods

S1.1 General Methods

All manipulations were conducted in an N_2-filled glovebox unless otherwise noted. Solvents were of reagent grade or higher purity. Aqueous HCl (12 M or 6 M) was sparged with N_2 for ca. 1 h before bringing into an N_2-filled glovebox for use. The solvent N,N'-dimethylformamide (DMF) was dried and degassed using the JC Meyer solvent purification system. All other reagents were purchased from commercial vendors and used as received. Powders of (EDBE)$CuCl_4$ were prepared as reported elsewhere.[1] Abbreviations used: BA = butylammonium, PCA = *p*-chloroanilinium, PEA = phenethylammonium, PA = propylammonium, DMF = N,N'-dimethylformamide, EtOH = ethanol.

As mentioned in the main text, the formula for **1$_{BA}$** was deduced through elemental analysis (Cu, In, C, H, N) with supporting evidence coming from XAS, EPR, and susceptibility measurements; the formulas for **1$_{PEA}$** and **1$_{PCA}$** are based on their analogy to **1$_{BA}$** (where only the organic cations are different).

S1.2 Synthesis of (PEA)$_4$[Cu^{II}(Cu^{I}In^{III})$_{0.5}$Cl$_8$] (1$_{PEA}$)

Solid CuCl (8.3 mg, 0.084 mmol), $CuCl_2$ (4.7 mg, 0.035 mmol), and In_2O_3 (15.9 mg, 0.0572 mmol), were combined with PEA•Cl (73.1 mg, 0.464 mmol) in 12 M HCl (1.35 mL). The mixture was stirred at 100 °C for 20 minutes affording a yellow solution. The solution was removed from the hot plate and cooled to room temperature, leading to the precipitation of a crop of black flake-like crystals. However, upon sitting in the mother liquor for 1-2 h, these black crystals were replaced primarily by a colorless solid. Re-dissolving these solids at 100 °C and quickly cooling the solution again led to formation of black crystals (but slowly cooling the solution at a controlled rate of ca. 5 °C/h afforded primarily colorless crystals with some ill-formed black and yellow solids). Single-crystal X-ray diffraction (SCXRD) studies of **1$_{PEA}$** were hindered by the poor crystallinity of crystals of **1$_{PEA}$** grown via air oxidation of the mother liquor of (PEA)$_4$Cu^{I}In^{III}Cl$_8$ (see main text Section 2.2) and via quickly cooling solutions of the precursors as described here. Furthermore, other characterization techniques were hindered by the instability of **1$_{PEA}$** in solution, which prevented isolation of phase pure samples.

S1.3 Synthesis of (BA)$_4$[Cu$^I_{0.5}$In^{III}Cl$_7$][Cu$^I_{0.5}$Cl][(BA)Cl]

Crystals of (BA)$_4$[Cu$_{0.5}$InCl$_7$][Cu$_{0.5}$Cl][(BA)Cl] suitable for SCXRD were prepared by combining CuCl (21.0 mg, 0.212 mmol), In_2O_3 (29.0 mg, 0.104 mmol), and butylamine (134 μL, 1.36 mmol), in 12 M HCl (0.5 mL). A small amount of H_3PO_2 (40 μL, 50 wt. % solution in H_2O) was added to reduce any trace amounts of Cu^{2+}. The solution was heated and stirred at 100 °C and all solids dissolved yielding a colorless solution. Slowly cooling the solution to room temperature at a controlled rate of 2 °C/h afforded colorless blade-like crystals.

S1.4 Synthesis of (BA)$_4$[Cu^{II}(Cu^{I}In^{III})$_{0.5}$Cl$_8$] (1$_{BA}$)

In order to assess the compositional variability of **1$_{BA}$** we prepared phase-pure samples (as determined by PXRD) via the two procedures given below, which use high and low precursor concentrations of Cu^{2+}.

S1.4.1 Synthesis of 1$_{BA}$ with a high precursor concentration of Cu^{2+}

Crystals of **1$_{BA}$** were prepared from a solution with a high precursor concentration of Cu^{2+} by combining CuCl (32.5 mg, 0.328 mmol), $CuCl_2$ (20.4 mg, 0.152 mmol), In_2O_3 (68.1 mg, 0.245 mmol), and butylamine

(204 μL, 2.06 mmol) in 12 M HCl (1.05 mL). The mixture was heated and stirred at 100 °C for 45 minutes and all solids dissolved affording a dark greenish-black solution. The solution was gradually cooled to room temperature by decreasing the temperature of the hot plate by 20 °C every 1 h yielding small black crystals that were collected by filtration on a glass frit and dried under reduced pressure for 20 h, affording 62.7 mg (0.0857 mmol) of $\mathbf{1_{BA}}$ (yield = 54.2%).[i] Anal. calcd. for $C_{16}H_{48}N_4Cu_{1.52}In_{0.48}Cl_8$: Cu: 13.20%, In: 7.53%, C: 26.26%, H: 6.61%, N: 7.66%. Found: Cu: 13.57%, In: 7.86%, C: 26.15%, H: 6.61%, N: 7.67%.

S1.4.2 Synthesis of $\mathbf{1_{BA}}$ with a low precursor concentration of Cu^{2+}

Crystals of $\mathbf{1_{BA}}$ were prepared from a solution with a low precursor concentration of Cu^{2+} by combining CuCl (45.5 mg, 0.460 mmol), $CuCl_2$ (5.7 mg, 0.0424 mmol), In_2O_3 (69.4 mg, 0.250 mmol), and butylamine (220 μL, 2.23 mmol) in 12 M HCl (1.4 mL). Following the above procedure (Section S1.4.1), the mixture was heated and stirred at 100 °C for 45 minutes and slowly cooled to room temperature. The solution was then allowed to sit undisturbed overnight yielding mm-scale black crystals that were collected by filtration on a glass frit and dried under reduced pressure for 20 h, affording 14.0 mg (0.0191 mmol) of $\mathbf{1_{BA}}$ (yield = 46.5%).[ii] These crystals were used for single-crystal conductivity measurements (Section S1.17). Anal. calcd. for $C_{16}H_{48}N_4Cu_{1.485}In_{0.515}Cl_8$: Cu: 12.83%, In: 8.07%. Found: Cu: 13.13%, In: 8.28%.

S1.4.3 Crystals of $\mathbf{1_{BA}}$ for SCXRD

Crystals of $\mathbf{1_{BA}}$ suitable for SCXRD were grown by dispersing a drop of the mother liquor from the reaction described in either Section S1.4.1 or S1.4.2 in Paratone-N® oil and allowing this mixture to sit in air for ca. 15 minutes. Small black crystals formed in the droplets of mother liquor and were quickly isolated for SCXRD measurements.

S1.5 Synthesis of $(PCA)_4[Cu^{II}(Cu^IIn^{III})_{0.5}Cl_8]$ ($\mathbf{1_{PCA}}$)

Crystals of $\mathbf{1_{PCA}}$ suitable for SCXRD were obtained by combining CuCl (9.7 mg, 0.098 mmol), $CuCl_2$ (4.8 mg, 0.036 mmol), In_2O_3 (18.3 mg, 0.0659 mmol), and PCA•Cl (73.9 mg, 0.579 mmol) in 6 M HCl (0.5 mL). The solids were dissolved by stirring at 100 °C for 10 minutes giving a dark greenish solution. Upon removing from the hot plate, black crystals formed throughout the solution within minutes. Within 4 h of their formation, crystals were isolated in Paratone and mounted for SCXRD collection. This haste was required because, similar to $\mathbf{1_{PEA}}$, crystals of $\mathbf{1_{PCA}}$ are slowly replaced by other phases (colorless crystals and green solid) over the course of 5-6 h. When this same hot solution is cooled slowly to room temperature, we observe formation of colorless and green solids only. These observations suggest that the black solid is the kinetic product but over time, converts to a number of side phases that are thermodynamically favored.

S1.6 Synthesis of $(PEA)_4Cu^IIn^{III}Cl_8$

Crystals of $(PEA)_4CuInCl_8$ suitable for single-crystal conductivity studies were prepared by combining CuCl (8.9 mg, 0.090 mmol), In_2O_3 (12.2 mg, 0.0439 mmol), and phenethylamine (85 μL, 0.676 mmol) in

---

[i] Percent yield calculated based on formula calculated from ICP-MS data $(BA)_4[(Cu^{II})_{1.04}(Cu^IIn^{III})_{0.48}Cl_8]$ (FW = 731.892 g/mol). See Section S2.4 for ICP-MS analysis.

[ii] Percent yield calculated based on formula calculated from ICP-MS data $(BA)_4[(Cu^{II})_{0.97}(Cu^IIn^{III})_{0.515}Cl_8]$ (FW = 733.11 g/mol). See Section S2.4 for ICP-MS analysis.

12 M HCl (1.1 mL). A small amount of H_3PO_2 (45 μL, 50 wt. % solution in H_2O) was added to reduce any trace amounts of Cu^{2+}. The solution was stirred at 100 °C for 5 minutes and all solids dissolved yielding a pale-yellow solution. Slowly cooling the solution to room temperature at a controlled rate of 1 °C/h yielded colorless plate-like crystals. The mother liquor was pipetted off and the crystals were washed twice with 0.5 mL of cold 6 M HCl containing 50 μL H_3PO_2 (50 wt. % solution in H_2O). The crystals were then dried under reduced pressure for 20 h.

S1.7 Synthesis of $(PCA)_2Cu^{II}Cl_4$
Under ambient atmospheric conditions, $CuCl_2$ (150 mg, 1.11 mmol) and PCA·HCl (365.8 mg, 2.23 mmol) were dissolved in MeOH (4 mL), yielding a clear yellow solution. The solvent was allowed to slowly evaporate over the course of 2 days leading to growth of plate-like yellow crystals. The crystals were isolated by filtration and dried under reduced pressure. The crystals were ground into a fine powder for EPR measurements.

S1.8 Synthesis of $(BA)_2Cu^{II}Cl_4$
Under ambient atmospheric conditions, $CuCl_2$ (109.1 mg, 0.8115 mmol) was dissolved in EtOH (2.2 mL) yielding a green solution. This solution was added to a colorless solution of butylamine (168 μL, 1.70 mmol) in EtOH (2.2 mL) while stirring, forming a dark green slurry. A 12 M aqueous solution of HCl (0.3 mL) was added dropwise to the slurry while stirring, causing all solids to dissolve and affording a bright green solution. With continued stirring, Et_2O (10 mL) was added, inducing precipitation of a yellow solid. The solid was isolated by centrifugation and then washed twice by resuspending in Et_2O (4 mL) and centrifuging to isolate the product. The product was then collected and dried under reduced pressure.

S1.9 Synthesis of $(PA)_2Cu^{II}Cl_4$
Crystals of $(PA)_2CuCl_4$ suitable for single-crystal conductivity studies were prepared by combining $CuCl_2$ (133.4 mg, 0.9922 mmol) and propylamine (200 μL, 2.43 mmol) in 6 M HCl (0.7 mL) under ambient atmospheric conditions. The mixture was stirred at 100 °C for 20 minutes yielding a green solution and then slowly cooled to room temperature at a controlled rate of 2 °C/h. The crystals were harvested by filtration on a glass frit and dried under reduced pressure for 12 h.

S1.10 Thin-film deposition
Thin films of 1_{BA} and $(BA)_2CuCl_4$ were prepared by spin coating a solution of the perovskite onto a glass substrate. Substrates were prepared by first scrubbing with an aqueous solution of Sparklean detergent and then sonicating for 15 minutes each in baths of aqueous Sparklean detergent solution, deionized water, acetone, and isopropanol. Substrates were removed from the isopropanol bath, promptly blown dry with compressed air, and treated with a 15-minute UV-ozone etch immediately prior to bringing them into an N_2-filled glovebox for film spinning.

S1.10.1 Thin-film deposition of 1_{BA}
A powder of 1_{BA} prepared as described in Section S1.4.1 (28.0 mg, 0.0383 mmol) was dissolved in DMF (109 μL) yielding a yellow-orange solution. The solution (20 μL) was deposited onto a glass substrate (1 cm^2) which was then spun at 500 rpm for 30 s (acceleration of 100 rpm/s) and then at 3000 rpm for 45 s (acceleration of 1000 rpm/s). The nearly colorless film was immediately annealed at 100 °C for 7 minutes,

causing it to turn a dark purple color, though yellow regions were also apparent (presumably corresponding to the Cu^{2+} perovskite. However, upon sitting in an N_2 atmosphere for 1 month, films adopted a uniform dark purple color and were analyzed by thin-film transmission spectroscopy and PXRD.

S1.10.2 Thin-film deposition of (BA)$_2$CuCl$_4$

A powder of (BA)$_2$CuCl$_4$ (28.0 mg, 0.0792 mmol) was dissolved in DMF (158 μL). The solution (15 μL) was deposited onto a glass substrate (1 cm^2) which was then spun at 3000 rpm for 40 s (acceleration of 200 rpm/s) and then at 5000 rpm for 70 s (acceleration of 2000 rpm/s). A stream of N_2 was directed into the top of the spin coater after the spinning rate reached 3000 rpm. Immediately after spinning, the film was annealed at 100 °C for 5 minutes yielding a yellow color.

S1.11 Crystal structure determination

Crystals of (BA)$_4$[Cu$^I_{0.5}$In^{III}Cl$_7$][Cu$^I_{0.5}$Cl][(BA)Cl] and **1$_{PCA}$** were stored in vials sealed under N_2 until immediately before the measurement. Then, under ambient atmospheric conditions, they were quickly removed from their mother liquor and immersed in Paratone-N® oil. Crystals of **1$_{BA}$** were grown inside a droplet of Paratone-N® oil immediately before the measurement, as described in Section S1.4.3. All crystals were promptly mounted on a Kapton® loop and transferred to a Bruker D8 Venture diffractometer equipped with a Photon II detector or to the Bruker D85 diffractometer at the Advanced Light Source beamline 12.2.1 at Lawrence Berkeley National Laboratory. In both cases, a flow of N_2 enveloped the mounted crystal. Frames were collected using ω and φ scans and unit-cell parameters were refined against all data. Crystals of (BA)$_4$[Cu$_{0.5}$InCl$_7$][Cu$_{0.5}$Cl][(BA)Cl] and **1$_{PCA}$** did not show significant decay during data collection, but for **1$_{BA}$**, the data quality diminished substantially over the course of the measurement. Frames were integrated and corrected for Lorentz and polarization effects using SAINT 8.34a and were corrected for absorption effects using SADABS V2014.[2] Space-group assignments were based upon systematic absences, *E*-statistics, agreement factors for equivalent reflections, and successful refinement of the structures. Structures were solved using the intrinsic phasing method implemented in APEX2.[2-3] Solutions were refined against all data using the SHELXTL-2013[4] software package and OLEX2.[3-6] Hydrogen atoms were inserted into the structure of **1$_{PCA}$** at idealized positions and refined using a riding model with an isotropic thermal parameter 1.2 times that of the attached carbon or nitrogen atom. Thermal parameters for all non-hydrogen atoms were refined anisotropically. The B site in **1$_{BA}$** and **1$_{PCA}$** was refined as a mixture of Cu and In. In the 300 K structure of **1$_{PCA}$**, the PCA cation was best modeled as disordered across two orientations related by a 90° rotation about the molecule's C_2 axis, while in the structure of (BA)$_4$[Cu$_{0.5}$InCl$_7$][Cu$_{0.5}$Cl][(BA)Cl] the position of one carbon atom of one of the five unique BA cations was modeled as disordered over two positions. Additional disorder of the organic molecules in (BA)$_4$[Cu$_{0.5}$InCl$_7$][Cu$_{0.5}$Cl][(BA)Cl] and in **1$_{BA}$** was treated by restraining some C–C bond lengths and C–C–C bond angles. Additionally, some C and N atoms were treated with rigid-bond and similar-ADP (atomic displacement parameter) restraints. Details regarding the data quality and a summary of the residual values of the refinements are listed in Table S1 and Table S2.

S1.12 Elemental Analysis

Inductively couple plasma mass spectrometry (ICP-MS) data were collected at the Stanford University Environmental Measurements Facility using a Thermo XSeries II ICP-Mass Spectrometer. In a typical procedure, powder of **1$_{BA}$** was dissolved in 4 mL of 17.5% aqueous HNO_3. The resulting solution was

diluted 12.5-fold with deionized water and filtered through glass filter paper to remove undissolved particulate. This stock solution was further diluted with 1.4% aqueous HNO_3 to prepare a series of samples for ICP-MS analysis of copper (Cu) and indium (In) content. C, H, and N analyses were performed by Midwest Microlab (Indianapolis, IN).

S1.13 Powder X-ray Diffraction (PXRD)
Powder X-ray diffraction (PXRD) measurements of powders of 1_{BA} and $(BA)_2CuCl_4$ were performed on a PANalytical X'Pert powder diffractometer with a Cu anode ($K\alpha_1 = 1.54060$ Å, $K\alpha_2 = 1.54443$ Å, $K\alpha_2/K\alpha_1 = 0.50000$), a programmable divergence slit with a nickel filter, and a PIXcel1D detector. The instrument was operated in a Bragg-Brentano geometry with a step size of 0.02° (2θ). PXRD measurements of films of 1_{BA} and $(BA)_2CuCl_4$ were performed on a Bruker D8 Advance diffractometer equipped with a Cu anode, fixed divergence slits with a nickel filter, and a LYNXEYE 1D detector. The instrument was operated in a Bragg-Brentano geometry with a step size of 0.01° or 0.004° (2θ). Samples of 1_{BA} were kept sealed under N_2 until immediately before the measurement but measurements were conducted in air. Repeated scans showed no signs of significant sample degradation over the course of 30 minutes. Simulated powder patterns were calculated using the CIFs from single-crystal X-ray experiments.

S1.14 Absorption measurements
Absorption measurements of thin films were taken using an Agilent Cary 6000i spectrometer. The thin film was placed directly in the beam path and the instrument was operated in transmission mode. Films of 1_{BA} were mounted inside of quartz cuvettes sealed under N_2 and this cuvette was placed in the beam path.

Diffuse reflectance measurements of powders were obtained using a Shimadzu UV-2600 spectrometer equipped with an integrating sphere. Finely ground powders were pulverized with $BaSO_4$ using a mortar and pestle to make a dilute mull. This mull was pressed into a pellet of $BaSO_4$ and used for diffuse reflectance measurements. Measurements of 1_{BA} were obtained under an N_2 atmosphere.

IR spectra were collected on a Thermo Nicolet 6700 FTIR spectrometer with a Smart Orbit attenuated total reflectance accessory. Spectra of 1_{BA} were acquired under an N_2 atmosphere.

S1.15 Electron paramagnetic resonance
X-band electron paramagnetic resonance (EPR) spectra were obtained with a Bruker EMX spectrometer, an ER 041 XG microwave bridge, and an ER4116DM cavity. Powders of 1_{BA} were sealed inside EPR tubes under an N_2 atmosphere while powders of $(BA)_2CuCl_4$ and $(PCA)_2CuCl_4$ were loaded into EPR tubes under ambient air. The masses of samples loaded for spin quantification measurements were carefully determined (Table S5). A sample temperature of 77 K was maintained using a liquid nitrogen finger dewar. The X-band EPR settings used to acquire the spectra shown in main text Figure 3A were as follows: frequency ≈ 9.42 GHz, power ≈ 1 mW, receiver gain = 22.4 dB, modulation frequency = 100 kHz, modulation amplitude = 4.0 G, time constant = 0.01 msec, conversion time = 5.12 msec. For spin quantification measurements, a power sweep was run to ensure that the signal was not saturated and to keep the quality factor (Q, the value of which indicates how efficiently the cavity stores microwave energy) the same for measurements of both 1_{BA} and the $(PCA)_2CuCl_4$ standard. This led to the following optimized parameters: frequency ≈ 9.40 GHz, power ≈ 0.0006 mW, receiver gain = 10 dB, modulation frequency = 100 kHz, modulation amplitude = 4.0

G, time constant = 0.01 msec, conversion time = 4.00 msec. Details of the spin quantification calculation are provided in Section S2.5.

S1.16 X-ray absorption spectroscopy (XAS)

X-ray absorption near-edge structure (XANES) spectra were collected at the K-edge of Cu at beamline 4-3 at the Stanford Synchrotron Radiation Lightsource (SSRL). Measurements were collected using both the fluorescence and total electron yield (TEY) techniques. Crystalline samples of 1_{BA}, $(PEA)_4CuInCl_8$, and $(EDBE)CuCl_4$ were ground using a mortar and pestle under an N_2 atmosphere. Samples for fluorescence measurements were prepared by sprinkling each powder into a cavity formed by 1 mm thick aluminum pallets backed with Kapton® tape to make a thin layer on the tape. The top of the sample cavity was then sealed with another piece of Kapton® tape and samples were kept sealed in glass jars under N_2 until they were transferred to the sample measurement chamber. Samples for TEY measurements were prepared by sprinkling each powder over a piece of conductive carbon tape under an He atmosphere and loading these samples directly into the measurement chamber. The sample measurement chamber was continuously purged with He to avoid sample decomposition and to reduce atmospheric absorption of the X-rays. We found that prolonged exposure of $(EDBE)CuCl_4$ to X-rays led to a spectrum that looked increasingly like that of the Cu^+ standard, indicating reduction of Cu^{2+}. As a result, collection times were minimized, and the shutter was closed between measurements to reduce sample X-ray exposure.

The spectra were analyzed using the Athena software package.[7] Each spectrum was energy-calibrated and then normalized by fitting the pre-edge region to a line and the post-edge to a cubic or quadratic polynomial. The effect of self-absorption on all samples measured was determined to be insignificant based on the near identity of their respective TEY and fluorescence spectra. TEY spectra are presented in the main text but these spectra are compared to the fluorescence data in Figure S5 to demonstrate this similarity. Each spectrum of 1_{BA} was fit by taking a linear combination of the spectra of the Cu^+ and Cu^{2+} standards in order to approximate the $Cu^+:Cu^{2+}$ ratio of 1_{BA}. These fits are shown in main text Figure 3C and Figure S6 and tabulated in Table S3.

S1.17 Electronic conductivity measurements

Crystals of 1_{BA}, $(PEA)_4CuInCl_8$, and $(PA)_2CuCl_4$ grow as relatively large (ca. 1 mm^2) thin (ca. 100-200 μm) flat plates according to the methods described in Sections S1.4.2, S1.6, and S1.9, respectively (Figure S11). Note that crystals of $(PA)_2CuCl_4$ were used for conductivity measurements because they grow as plates similar in thickness to 1_{BA} and $(PEA)_4CuInCl_8$, whereas crystals of $(BA)_2CuCl_4$ are extremely thin and delicate. Crystals were fixed to a sapphire substrate using a drop of a solution of poly(methylmethacrylate) (PMMA) in toluene. We used carbon contacts for all measurements in order to avoid electrochemical reactions between our halide-containing materials and metal contacts and to ensure that the measured conductivities correspond to electron transport, not ion transport, since graphite is an ion blocking electrode. A slurry of graphite in toluene was prepared from the commercially available PELCO colloidal graphite/isopropanol slurry (Ted Pella) by removing the isopropanol under reduced pressure then resuspending the graphite in toluene. A small paintbrush was used to apply this slurry to form two carbon contacts on each crystal. The crystal was mounted in a home-built probe station[8] and the tip of a stainless-steel probe painted with the same graphite suspension was pressed onto each contact. These manipulations

were carried out inside an N_2-filled glovebox for crystals of 1_{BA} and $(PEA)_4CuInCl_8$ and in ambient air for crystals of $(PA)_2CuCl_4$.

Electronic resistivity measurements were performed using a BioLogic VSP 300 potentiostat on samples inside an N_2-filled glovebox and enclosed by a small Faraday cage. For all measurements, the resistance between the two probes was measured using potentiostatic electrochemical impedance spectroscopy (PEIS). For crystals of $(PEA)_4CuInCl_8$ and $(PA)_2CuCl_4$, an AC voltage with a fixed amplitude of ± 1 V was applied and swept from a frequency of 200 MHz to ca. 10 mHz. For crystals of 1_{BA}, an AC voltage with a fixed amplitude of ± 0.5 V, ± 0.75 V, or ± 1 V was applied and swept from a frequency of 200 MHz to ca. 50 mHz. Measurements were run at a range of temperatures between 27 °C and 88 °C, and a thermocouple placed directly on the sample stage was used to monitor the sample temperature. Between measurements, the sample sat for at least 1 h to equilibrate to the new temperature.

The length (l) and width (w) of each crystal (used to calculate conductivity, Section S2.8) were estimated from pictures calibrated with a scale bar (Figure S11), while the thickness (t) was measured using an AccuRemote digital micrometer IP65. Crystal dimensions for a representative set of measured samples are included in Figure S11. Some crystals were oddly shaped, and we measured both a maximum and minimum length and/or width. Using these dimensions, we calculated the maximum and minimum conductivity values at each temperature point and the average of these values is reported in Table S6 for three crystals of 1_{BA}.

S1.18 Magnetic measurements

Finely ground powders of 1_{BA} were enclosed in plastic wrap under an N_2 atmosphere and quickly transferred to a Quantum Design Physical Properties Measurement System (PPMS) where they were purged with He gas and measured under vacuum. DC magnetization and DC and AC susceptibility measurements were performed from $T = 2–300$ K in applied fields up to $\mu_0H = 5$ T. AC susceptibility was measured with a 1.5 Oe drive current at a frequency of 9984 Hz. A sample consisting of thin plate-like crystals of 1_{BA} was prepared and transferred to the PPMS in the same manner. Frequency-dependent AC susceptibility measurements were performed from $T = 2–30$ K and 359–9984 Hz in zero applied field. The drive current was 5 Oe for frequencies less than 2000 Hz and 1.5 Oe for frequencies greater than 2000 Hz.

S2 Supplementary Discussion

S2.1 SCXRD structure of $(BA)_4[Cu_{0.5}InCl_7][Cu_{0.5}Cl][(BA)Cl]$

SCXRD reveals that the structure of $(BA)_4[Cu_{0.5}InCl_7][Cu_{0.5}Cl][(BA)Cl]$ is distinct from that of the 2D double perovskite $(PEA)_4CuInCl_8$ (main text Figure 2A) and from the layered perovskite $(BA)_2Cu_{0.5}In_{0.5}Cl_4$ reported recently.[9] The structure consists of stacked 1D ribbons of corner-sharing $[CuCl_6]^{5-}$ and $[InCl_6]^{3-}$ units (Figure S1A) and bears some resemblance to several recently reported 1D Cu^IBi^{III} materials.[10] Each ribbon is three octahedra wide with the two B-site cations arranged in an alternating checkerboard-like fashion, where In^{3+} and Cu^+ cations occupy the edge and center positions, respectively. The six-fold coordinated Cu^+ cations adopt a $2 + 4$ coordination with two short axial Cu–Cl bonds (2.1578(1) Å) perpendicular to the plane of the ribbons and four long equatorial Cu–Cl bonds (3.0287(1) Å and 3.0386(1) Å) lying in the plane of the sheet (Figure S1A, inset). This coordination environment is similar to those adopted by Cu^+ and other d^{10} transition metal cations in a range of perovskites[11-14] including $(PEA)_4CuInCl_8$

(main text Figure 2A, inset).[15] The ribbon structure of $(BA)_4[Cu_{0.5}InCl_7][Cu_{0.5}Cl][(BA)Cl]$ can be derived from the inorganic lattice of $(PEA)_4CuInCl_8$ by removing every other column of $[CuCl_2]^-$ units lying along the (011) direction (Figure S1B). Adjacent ribbons run parallel to one another, but their edges are offset, forming step-like layers. Interestingly, the $[CuCl_2]^-$ units that are missing from the perovskite lattice are found in the space between the ribbon layers along with BA cations and an additional Cl^- anion, yielding an overall formula of $(BA)_4[Cu_{0.5}InCl_7][Cu_{0.5}Cl][(BA)Cl]$. We have expressed this formula to demonstrate the analogy between this and the $A_4BB'X_8$ 2D double perovskite structure: half of the $[CuCl_2]^-$ units have been relocated away from the extended inorganic lattice, severing 2D connectivity, and an additional BA•Cl unit has been introduced into the structure.

S2.2 Additional notes on the SCXRD structure of 1_{BA}

Poor crystallinity and diffraction damage led to relatively low data quality for 1_{BA} at 300 K. Upon cooling, the number of spots in the diffraction pattern increased significantly and attempts to solve the data suggested either twinning or modulation of the structure. As described in Section S1.4.3, crystals of 1_{BA} that afforded the best data sets were those grown by the in-situ oxidation of the mother liquor. Importantly, the powder X-ray diffraction (PXRD) pattern simulated from the SCXRD data of a crystal grown via oxidation of the mother liquor matches the PXRD pattern of crystals grown via solution-state synthesis (Figure S18). This confirms that crystals grown using these two approaches are the same material and that solution-state synthesis affords phase-pure material.

Because of the relatively low data quality for 1_{BA}, we do not carry out an in-depth analysis of this structure in the main text, relying instead on the higher-quality data obtained for 1_{PCA} to understand the structure of the black perovskite phase. Nevertheless, it is important to note that the structural parameters obtained from 1_{BA} are consistent with our XAS and ICP-MS data for 1_{BA} and with the structure of 1_{PCA}. The B-site occupancy refines to give an overall Cu:In ratio of ca. 78:22 Cu:In (Table S1), very similar to our ICP-MS results (which give a ratio of ca. 75:25, Section S2.4) and also consistent with our XAS data (Section S2.3). The B-site occupancy ratio is also close to that obtained for 1_{PCA} (Table S2) and we find similar structural parameters (Figure S3). In particular, the B sites have short axial bonds of 2.3075(2) Å and 2.2996(2) Å (compared to 2.2790(1) Å in the 300 K structure of 1_{PCA}) and longer equatorial bonds of 2.6580(2) Å, 2.6656(2) Å, and 2.6924(2) Å (compared to 2.6600(1) Å and 2.6593(1) Å in the 300 K structure of 1_{PCA}). Additionally, the thermal displacement parameters of the equatorial halides are elongated along the directions of B–Cl–B connectivity an expected result of averaging the Cu^+, Cu^{2+}, and In^{3+} coordination spheres (main text Section 2.4).

S2.3 Estimating the formula of 1_{BA} from XAS data

If we assume that all Cu^+ is charge balanced by an equal amount of In^{3+}, we can use our XAS results to extract an approximate formula for 1_{BA}. For a $Cu^+:Cu^{2+}$ ratio of 25:75 (the approximate midpoint of the observed range, see Table S3), we obtain a formula of $(BA)_4[(Cu^{II})_{1.2}(Cu^IIn^{III})_{0.4}Cl_8]$, in which 60% of the Cu^+ and In^{3+} B-site cations of the Cu^+–In^{3+} double perovskite structure have been replaced with Cu^{2+}. However, it is worth emphasizing that these numbers obtained from XAS are merely an estimate as they rely on fits that assume that the Cu^+ and Cu^{2+} environments in 1_{BA} are identical to those in our Cu^+ and Cu^{2+} standards. Indeed, we do not see perfect agreement between the shape of our linear combination fits and

the experimental spectra of 1_{BA} main text Figure 3C and Figure S6). While the formula estimates based on XAS data (Table S3) are in reasonable agreement with those obtained by ICP-MS, we give much more weight to the ICP-MS derived formula, as ICP-MS is a more accurate technique for such analysis.

S2.4 Estimating the formula of 1_{BA} from ICP-MS data

We used ICP-MS to quantify the weight percent (wt.%) of Cu and In in two separate samples of 1_{BA} (prepared using high and low concentrations of Cu^{2+}, see Section S1.4) and our results are tabulated in Table S4. To calculate the overall composition of each sample from these results, we assumed a general formula of $(BA)_4[Cu^{II}_x(Cu^I In^{III})_y Cl_8]$ where $x + 2y = 2$. In other words, we assume the material maintains charge neutrality by incorporating equal amounts of In^{3+} and Cu^+. To find the formula that is most consistent with both the Cu and In wt.% values obtained by ICP-MS, we use the ratio of the Cu wt.% to the In wt.% (rather than using the individual wt.% values) to solve for x and y. The Cu wt.% can be expressed as:

$$Cu\ wt.\% = \frac{63.546 \times (x + y)}{FW} \qquad \text{Equation S1}$$

where FW is the weight of one formula unit of 1_{BA}. Similarly, the In wt.% can be expressed as:

$$In\ wt.\% = \frac{114.82 \times y}{FW} \qquad \text{Equation S2}$$

Taking the ratio of the two, we obtain:

$$\frac{Cu\ wt.\%}{In\ wt.\%} = \frac{63.546 \times (x + y)}{114.82 \times y} = (0.55)\frac{x + y}{y} \qquad \text{Equation S3}$$

Then, using the assumption that $x + 2y = 2$, we can re-express this as:

$$\frac{Cu\ wt.\%}{In\ wt.\%} = (0.55)\frac{1 + \frac{x}{2}}{1 - \frac{x}{2}} \qquad \text{Equation S4}$$

This equation enables us to solve for x using the values of the Cu and In wt.% obtained from ICP-MS. Plugging this value of x into the expression $x + 2y = 2$, we find y. Values of x, y, and the overall formula for the two samples of 1_{BA} measured using ICP-MS are given in Table S4. Despite the very different amounts of Cu^{2+} used in their synthesis, the two samples have remarkably similar empirical formulas leading us to propose the approximate formula of $(BA)_4[Cu^{II}(Cu^I In^{III})_{0.5}Cl_8]$ for 1_{BA}.

S2.5 Estimating the Cu^{2+} content of 1_{BA} using EPR

EPR spectra of 1_{BA} and $(PCA)_2CuCl_4$ (obtained as specified in Section S1.15) were used to estimate the amount of Cu^{2+} in 1_{BA}. The raw (first derivative) spectra (Figure S4A,C) were integrated (giving the absorption spectra), and the resulting spectra were baseline corrected using a spline function (OriginPro, Figure S4B,D). The integral of these spectra (blue shaded area in Figure S4B,D) gives the value of the signal intensity (V_s, Table S5). As shown in Equation S5, V_s can be expressed in terms of η and Z_0 (instrument parameters that are constant for all measurements), χ'' (the magnetic susceptibility), Q (the quality factor), and P (the power).[16]

$$V_s = \chi'' \eta Q \sqrt{PZ_0} \qquad \text{Equation S5}$$

Since the only magnetic component in both 1_{BA} and $(PCA)_2CuCl_4$ is Cu^{2+} ($S = \frac{1}{2}$), the value of χ'' is proportional to the amount of Cu^{2+} (n_{Cu2+}) in the sample, allowing us to write:

$$V_s \sim (n_{Cu^{2+}})\eta Q\sqrt{PZ_0}$$

Equation S6

Thus, we can use the ratio of the V_s values determined for 1_{BA} and $(PCA)_2CuCl_4$ to determine the amount of Cu^{2+} in the sample of 1_{BA} by using the known amount of Cu^{2+} in the sample of $(PCA)_2CuCl_4$ (Table S5) in Equation S7:

$$\frac{V_{s(standard)}}{V_{s(1_{BA})}} \sim \frac{(n_{Cu^{2+}((PCA)_2CuCl_4)})\sqrt{P_{((PCA)_2CuCl_4)}}}{(n_{Cu^{2+}(1_{BA})})\sqrt{P_{(1_{BA})}}}$$

Equation S7

In this way, we calculate a Cu^{2+} weight% value for 1_{BA} of 7.79% (Table S5). Given the many potential sources of error inherent to EPR spin quantification[17] this value is in good agreement with the Cu^{2+} weight% calculated using the formula $(BA)_4[Cu^{II}(Cu^{I}In^{III})_{0.5}Cl_8]$ (8.67%) derived from ICP-MS data (Section S2.4).

S2.6 Estimating the amount of Cu^{2+} using magnetic susceptibility data

Since Cu^{2+} is the only magnetic component of 1_{BA}, we can also use our magnetic susceptibility data to estimate the amount of Cu^{2+} present in 1_{BA}. The measured high-temperature, high-field DC moment data of 1_{BA} were converted to magnetic susceptibility (χ) using the molecular weight of the idealized formula unit (f.u.) for $(BA)_4[(Cu^{II})(Cu^{I}In^{III})_{0.5}Cl_8]$ (732.933 g/mol) (main text Figure 6B). A large temperature-independent diamagnetic contribution was identified and subtracted ($\chi_0 = -0.00108$ emu/mol), and then a Curie-Weiss fit was carried out on the inverse susceptibility data $((\chi-\chi_0)^{-1})$ to extract the Curie constant (C) and Weiss temperature (Θ):

$$\frac{1}{\chi - \chi_0} = \frac{1}{C}T - \frac{\Theta}{C}$$

Equation S8

The susceptibility per formula unit ($\chi_{f.u.}$) is related to the susceptibility per magnetic ion (χ_m) by:

$$\chi_m = \frac{1}{n_m}\chi_{f.u.}$$

Equation S9

where n_m is the number of magnetic ions in the formula unit). Substituting this relationship into the Curie-Weiss law expressed in terms of $\chi_{f.u.}$:

$$\chi_{f.u.} = \frac{C_{f.u.}}{T - \Theta} + \chi_{0,f.u.}$$

Equation S10

(where $C_{f.u.}$ is the Curie constant per formula unit) allows us to determine that a similar relationship exists for the Curie constant:

$$C_m = \frac{1}{n_m}C_{f.u.}$$

Equation S11

(where C_m is the Curie constant per magnetic ion). The Curie-Weiss fit described above was performed using $\chi_{f.u.}$ data and thus determined the value of $C_{f.u.}$. Combining the relationship:

$$\mu_{eff} = \sqrt{8 \times C}$$

Equation S12

(where μ_{eff} is the effective magnetic moment) with Equation S11, we obtain:

$$\mu_{eff} = \sqrt{8\frac{C_{f.u.}}{n_m}} \qquad \textbf{Equation S13}$$

We assume an expected effective moment (μ_{eff}) for Cu^{2+} of 1.73 μ_B (spin only value for $S = \frac{1}{2}$), enabling us to solve Equation S13 for n_m by using $C_{f.u.}$. This analysis resulted in a value of $n_m = 0.97$, which indicates that there is approximately one Cu^{2+} per formula unit. This is in good agreement with our XAS, ICP-MS, and EPR spin quantification data (Sections S2.3, S2.4, S2.5) which indicate that 50% of the B sites are occupied by Cu^{2+} (i.e., $n_m = 1$) giving an approximate formula of $(BA)_4[(Cu^{II})(Cu^{I}In^{III})_{0.5}Cl_8]$.

S2.7 Packing of distorted octahedra

In main text Section 2.5, we describe how a cell composed of one $[In^{III}Cl_6]^{3-}$, one $[Cu^{I}Cl_6]^{5-}$, and two $[Cu^{II}Cl_6]^{4-}$ units can be tessellated to generate a 2D perovskite lattice with little packing mismatch. A unique lattice with even less packing mismatch can be produced from this same cell by translating along one direction while rotating 180° and then translating along the orthogonal direction (Figure S9B). In fact, an array of unique lattices can be generated by carrying out reflections or rotations on this cell followed by translations (Figure S9). However, not all of these lattices are expected to be equally favorable. Those pictured in Figure S9D-F exhibit much greater packing mismatch than those in Figure S9B,C (as highlighted by the colored ovals) suggesting that they are less favorable. Those containing adjacent In^{3+} cations (Figure S9E,F) should be further disfavored due to the electrostatic repulsion of highly charged cations.

Compositions that deviate significantly from 50% Cu^{2+} and 25% each of Cu^+ and In^{3+}, will introduce an increasing number of clusters like those shown in Figure S8 into the lattice. As indicated by the colored circles, these clusters are expected to introduce significant packing mismatch, thus suggesting that substantial deviation from a 1:2:1 $Cu^+:Cu^{2+}:In^{3+}$ ratio of B-site cations is unfavorable. Notably, this explains the experimentally observed ratios.

S2.8 Conductivity calculations

Conductivity (σ) values were extracted from the Nyquist plots (Section S1.17) using the following equation:

$$\sigma = \frac{1}{\rho} = \frac{l}{R*A} = \frac{l}{R*(w*t)} \qquad \textbf{Equation S14}$$

where ρ is the resistivity, R is the resistance at the DC limit, A is the cross-sectional area of the crystal, l is the distance between the two contacts on the crystal, and w and t represent the crystal's width and thickness, respectively. The value of R was approximated from the Nyquist plot as shown in Figure S13.

Two crystals each of both $(PEA)_4CuInCl_8$ and $(PA)_2CuCl_4$ were measured at ambient temperature (ca. 28 °C), and, as shown in the Nyquist plots in Figure S12, these materials were too insulating to extract meaningful values of resistivity. Three crystals of $\mathbf{1_{BA}}$ were measured at a range of temperatures between 27 °C and 88 °C (Table S6). At room temperature the average conductivity for these three crystals is 8×10^{-9} S/cm.

S2.9 Activation energy calculations

The activation energy (E_a) for conduction in $\mathbf{1_{BA}}$ was estimated from the slope of a plot of $\ln(\sigma)$ vs. $1/T$ (T = temperature) according the Arrhenius equation:

$$\ln(\sigma) = \ln(A) - \left(\frac{E_a}{k_B}\right)\left(\frac{1}{T}\right)$$

Equation S15

where A is a constant and k_B is the Boltzmann constant. Raising the sample temperature substantially above ca. 70 °C for prolonged periods caused the temperature dependence of σ to deviate from the Arrhenius behavior displayed at lower temperatures, increasing more quickly than expected at higher temperature (Figure S14). Upon returning to room temperature, a crystal exposed to this extreme heat treatment (crystal 1) was found to be significantly more conductive than before heating, and the conductivity did not return to its original value (Figure S13), indicating an irreversible change in the crystal. For this reason, in order to ensure we were extracting a reliable value for E_a, all further samples we measured were heated only over a narrow range between 27 °C and 51 °C. In addition, after progressing through a series of increasing temperatures, crystals were re-measured at several lower temperatures to ensure reversibility. The σ values for two additional crystals of $\mathbf{1_{BA}}$ (crystals 2 and 3) are given in Table S6 and Arrhenius plots along with E_a values extracted from them are shown in Figure S15. The values of E_a for crystals 2 and 3 (571 meV and 635 meV, respectively) are in good agreement with that extracted from the low-temperature region for crystal 1 (609 meV, Figure S14). Averaging the three values, we find $E_a \sim 600$ meV.

S2.10 IVCT peak analysis

Because diffuse reflectance measurements can easily be skewed by the extreme sensitivity of this technique to weak absorption events,[11, 18] we instead used the thin-film transmission spectrum of $\mathbf{1_{BA}}$ to analyze the IVCT absorption feature of this material. Figure S16 shows that the thin-film spectrum is well fit by two Gaussian peaks of the form:

$$y = y_0 + \frac{A}{w \times \sqrt{\pi/2}} e^{-2 \times \left[\frac{x-x_c}{w}\right]^2}$$

Equation S16

where the parameters y_0, x_c, w, and A correspond to the peak's y offset, center position along the x axis, full width at half maximum, and area, respectively (see Table S7 for the fitted values of these parameters). These Gaussian peaks, centered at 2.28 and 3.31 eV, describe the IVCT and LMCT features, respectively. As discussed in main text Section 2.6.2, the energy of the IVCT feature (2.28 eV) is approximately four times larger than the activation energy for conductivity (ca. 0.6 eV), suggesting that a $Cu^+ \rightarrow Cu^{2+}$ charge hopping pathway is responsible for the electronic conductivity.

S3 Additional Figures and Tables

Table S1 Crystallographic data for $(BA)_4[Cu_{0.5}InCl_7][Cu_{0.5}Cl][(BA)Cl]$ and **1$_{BA}$**.

Compound	$(BA)_4[Cu_{0.5}InCl_7][Cu_{0.5}Cl][(BA)Cl]$	**1$_{BA}$**
Empirical Formula	$C_{20}Cl_9CuInN_5$	$C_{16}Cl_8Cu_{1.55}In_{0.45}N_4$
Formula Weight, g/mol	807.66	681.96
Temperature, K	300	300
Crystal System	Monoclinic	Triclinic
Space group	$C2/c$	$P–1$
a, Å	32.2043(12)	7.4458(6)
b, Å	7.6774(3)	7.6348(6)
c, Å	34.1813(13)	15.5065(15)
α, °	90	89.970(6)
β, °	107.203(2)	76.106(6)
γ, °	90	89.921(5)
Volume, Å^3	8073.1(5)	855.71(13)
Z	8	1
Density (calculated), g/cm3	1.329	1.323
Absorption coefficient, mm^{-1}	1.815	2.023
$F(000)$	3088.0	327.0
Crystal size, mm^3	$0.1 \times 0.05 \times 0.015$	$0.07 \times 0.04 \times 0.005$
Radiation	Synchrotron ($\lambda = 0.7288$ Å)	Synchrotron ($\lambda = 0.7288$ Å)
2θ range, °	2.558 to 56.696	5.78 to 52.084
Index ranges	$-41 \leq h \leq 41$ $-9 \leq k \leq 9$ $-44 \leq l \leq 44$	$-8 \leq h \leq 8$ $-9 \leq k \leq 9$ $-18 \leq l \leq 18$
Reflections collected/unique	64719/9323	10976/3085
Completeness to θ_{max}	0.998	0.985
Max. and min. transmission	0.431, 0.384	0.429, 0.266
Data/restraints/parameters	9323/150/337	3085/68/141
Goodness-of-fit on F^2	1.047	1.090
Final R indices [$I > 2\sigma(I)$][a]	$R_1 = 0.0507$ $wR_2 = 0.1587$	$R_1 = 0.0905$ $wR_2 = 0.2586$
R indices (all data)[a]	$R_1 = 0.0603$ $wR_2 = 0.1736$	$R_1 = 0.1145$ $wR_2 = 0.2790$
Largest diff. peak and hole, e/Å^{-3}	1.40, −1.36	0.69, −0.92

[a]$R_1 = \Sigma||F_o| - |F_c||/\Sigma|F_o|$, $wR_2 = [\Sigma w(F_o^2 - F_c^2)^2/\Sigma(F_o^2)^2]^{1/2}$

Table S2 Crystallographic data for **1$_{PCA}$** at 300 and 100 K.

Compound	1$_{PCA}$ (300 K)	1$_{PCA}$ (100 K)
Empirical Formula	C$_{12}$H$_{14}$Cl$_6$Cu$_{0.83}$In$_{0.17}$N$_2$	C$_{12}$H$_{14}$Cl$_6$Cu$_{0.78}$In$_{0.22}$N$_2$
Formula Weight, g/mol	471.21	473.77
Temperature, K	300	100
Crystal System	Monoclinic	Orthorhombic
Space group	$P2_1/c$	$Pccn$
a, Å	16.4410(8)	7.4183(4)
b, Å	7.5928(4)	32.1336(18)
c, Å	7.3130(4)	7.2590(4)
α, °	90	90
β, °	102.684(2)	90
γ, °	90	90
Volume, Å^3	890.63(8)	1730.38(16)
Z	2	4
Density (calculated), g/cm3	1.757	1.819
Absorption coefficient, mm^{-1}	2.274	2.204
F(000)	469.0	942.0
Crystal size, mm^3	0.13 × 0.085 × 0.01	0.075 × 0.05 × 0.005
Radiation	Synchrotron ($\lambda = 0.7288$ Å)	MoKα ($\lambda = 0.71073$ Å)
2θ range, °	5.208 to 61.758	5.07 to 54.226
Index ranges	$-23 \leq h \leq 23$ $-10 \leq k \leq 10$ $-10 \leq l \leq 10$	$-9 \leq h \leq 9$ $-41 \leq k \leq 41$ $-9 \leq l \leq 9$
Reflections collected/unique	29270/2613	24089/1915
Completeness to θ$_{max}$	1.000	1.001
Max. and min. transmission	0.434, 0.374	0.430, 0.350
Data/restraints/parameters	2613/0/136	1915/0/99
Goodness-of-fit on F^2	1.091	1.215
Final R indices [$I > 2\sigma(I)$][a]	$R_1 = 0.0490$ w$R_2 = 0.1244$	$R_1 = 0.0777$ w$R_2 = 0.1388$
R indices (all data)[a]	$R_1 = 0.0503$ w$R_2 = 0.1250$	$R_1 = 0.0908$ w$R_2 = 0.1434$
Largest diff. peak and hole, e/Å^{-3}	1.03, −1.02	1.47, −1.53

[a]$R_1 = \Sigma||F_o| - |F_c||/\Sigma|F_o|$, w$R_2 = [\Sigma w(F_o^2 - F_c^2)^2/\Sigma(F_o^2)^2]^{1/2}$

Table S3 Values of Cu^{2+} and Cu^+ content for two samples of **1$_{BA}$** prepared using high and low Cu^{2+} precursor concentrations (Section S1.4) obtained from linear combination fits of the TEY and fluorescence XAS data (Figure S6 and main text Figure 3C). See Section S2.3 for full analysis.

Sample	XAS method	% Cu^{2+}	% Cu^+	Approximate Formula
1$_{BA}$ (high Cu^{2+} concentration)	TEY	78.3 %	21.7 %	$(BA)_4[(Cu^{II})_{1.3}(Cu^{I}In^{III})_{0.35}Cl_8]$
	Fluorescence	79.8 %	20.2 %	
1$_{BA}$ (low Cu^{2+} concentration)	TEY	72.5 %	27.5 %	$(BA)_4[(Cu^{II})_{1.14}(Cu^{I}In^{III})_{0.43}Cl_8]$
	Fluorescence	74.4 %	25.6 %	

Table S4 Values of weight percent (wt. %) obtained for two samples of **1$_{BA}$** (prepared using high and low Cu^{2+} precursor concentrations, see Section S1.4) using ICP-MS. The ratio of Cu wt. % to In wt. % was used to determine the values of x and y in the generic formula $(BA)_4[Cu^{II}_x(Cu^{I}In^{III})_yCl_8]$ (Section S2.4), giving the calculated formula listed.

	Cu wt. %	In wt. %	Cu wt. % ÷ In wt. %	x	y	Calculated Formula
1$_{BA}$ (high Cu^{2+} concentration)	13.57	7.86	1.73	1.04	0.48	$(BA)_4[(Cu^{II})_{1.04}(Cu^{I}In^{III})_{0.48}Cl_8]$
1$_{BA}$ (low Cu^{2+} concentration)	13.13	8.28	1.59	0.97	0.515	$(BA)_4[(Cu^{II})_{0.97}(Cu^{I}In^{III})_{0.515}Cl_8]$

Table S5 Table of parameters and quantities used in the EPR spin quantification of Cu^{2+} in **1$_{BA}$** (Section S2.5). (V_s = signal intensity, P = power, and Q = quality factor.) The number of moles of Cu^{2+} present in the $(PCA)_2CuCl_4$ sample is known and was used to calculate the number of moles of Cu^{2+} in the sample of **1$_{BA}$**.

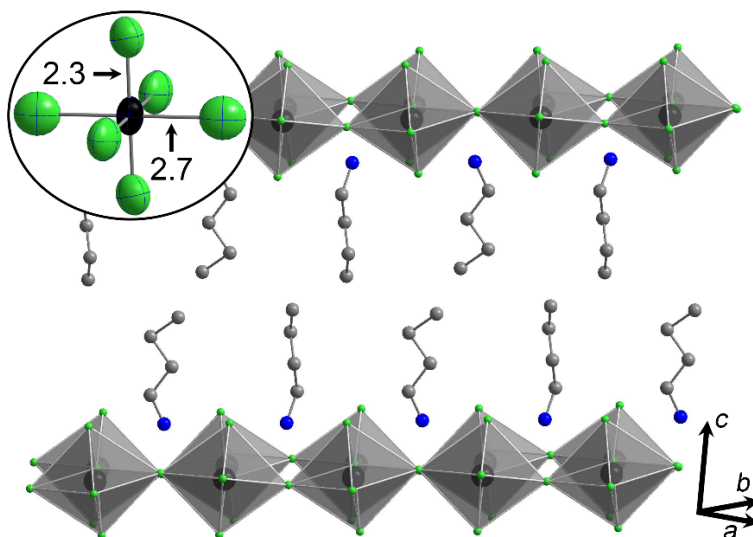|	$(PCA)_2CuCl_4$	**1$_{BA}$**
Mass of sample	0.1960 g	0.2084 g
V_s	2.355×10^{11}	1.419×10^{11}
P	0.0006291 mW	0.0006307 mW
Q	6600	6600
Moles Cu^{2+}	4.24×10^{-4} mol (known)	2.55×10^{-4} mol (calculated)
Weight % Cu^{2+}	13.75% (known)	7.79% (calculated)

Table S6 Conductivity values for three crystals of 1_{BA} measured at a range of temperatures. The Arrhenius plots for these crystals are given in Figure S14 and Figure S15. Temperature points are listed from top to bottom in the order in which they were measured. Values shown in red for crystal 1 were not used for the E_a calculation as the crystal irreversibly changed upon heating above ca. 70 °C (Figure S13).

| 1_{BA} – crystal 1		1_{BA} – crystal 2		1_{BA} – crystal 3	
Temperature (°C)	Conductivity (S/cm)	Temperature (°C)	Conductivity (S/cm)	Temperature (°C)	Conductivity (S/cm)
28	6.44×10^{-9}	28	1.27×10^{-8}	30	5.20×10^{-9}
50	3.09×10^{-8}	34	1.88×10^{-8}	35	7.20×10^{-9}
63	7.48×10^{-8}	41	3.25×10^{-8}	42	1.25×10^{-8}
77	2.39×10^{-7}	51	6.25×10^{-8}	51	2.64×10^{-8}
88	7.05×10^{-7}	38	2.70×10^{-8}	45	1.72×10^{-8}
27	2.02×10^{-8}	29	1.50×10^{-8}	27	4.42×10^{-9}

Table S7 Fitting parameters for Gaussian fits of the IVCT and LMCT features in the thin film transmission spectrum of 1_{BA}. The parameters y_0, x_c, w, and A correspond to the peak's y offset, center position along the x axis, full width at half maximum, and area. The function used for the fit is defined in Equation S16.

	IVCT	LMCT
y_0	0.00329	0.00329
x_c	2.28244	3.30953
w	0.83168	0.60164
A	0.77508	0.71369

Figure S1 (A) SCXRD structure of $(BA)_4[Cu_{0.5}InCl_7][Cu_{0.5}Cl][(BA)Cl]$ with an inset showing the local coordination of the Cu^+ cations in the 1D ribbons. (B) $n = 1$ perovskite sheet of $(PEA)_4CuInCl_8$ (left)[15] showing how removal of every other column of $[CuCl_2]^-$ units along the (011) direction affords the inorganic lattice of $(BA)_4[Cu_{0.5}InCl_7][Cu_{0.5}Cl][(BA)Cl]$ (right). Turquoise, red, green, gray, and blue spheres represent Cu^+, In^{3+}, Cl, C, and N atoms, respectively. H atoms were not included in the refinement.

Figure S2 Time lapse photographs taken with a microscope camera showing the growth of crystals of **1$_{BA}$** observed over the course of ca. 4 minutes when an HCl solution containing Cu^+, In^{3+}, and butylammonium precursors is placed in a drop of Paratone-N® oil and left to sit in air (see Section S1.4.3).

Figure S3 Room temperature SCXRD structure of **1$_{BA}$**. The inset shows the local coordination environment of the B site. Green, blue, and gray spheres represent Cl, N, and C atoms, respectively. Black spheres represent mixed Cu/In sites. H atoms were not included in the refinement due to the relatively low data quality.
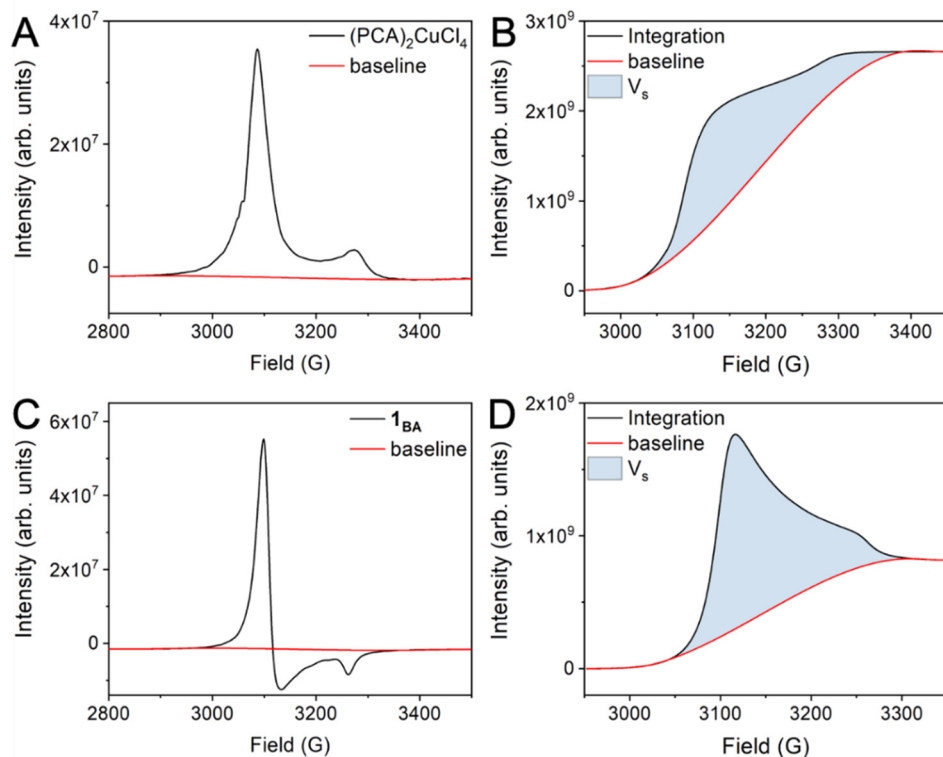

Figure S4 EPR spectra for (A) (PCA)$_2$CuCl$_4$ (power = 0.0006291 mW) and (C) **1$_{BA}$** (power = 0.0006307 mW) and the integrated spectra for (B) (PCA)$_2$CuCl$_4$ and (D) **1$_{BA}$**. The value of V_s (the integration value of the spectra in B and D) is represented by the blue shaded area and is proportional to the amount of Cu^{2+} in each sample.
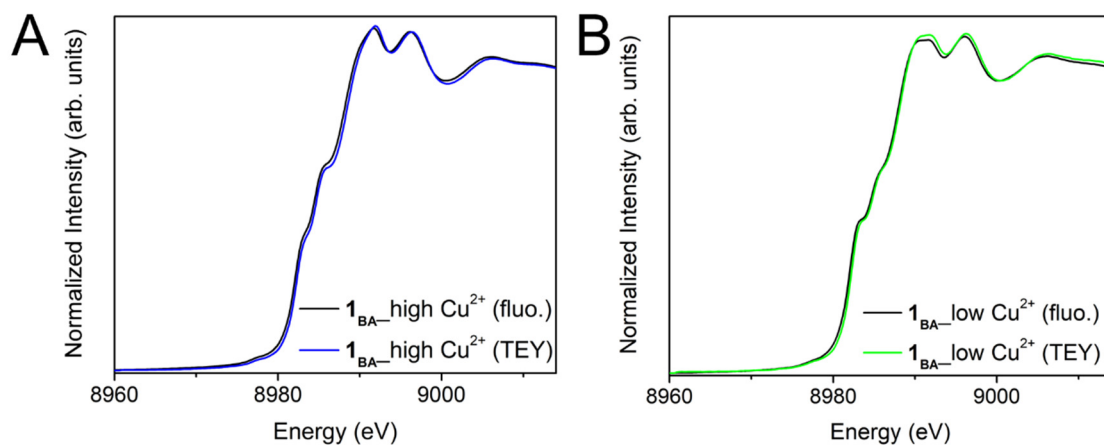
Figure S5 (A) XAS data for a sample of **1**$_{BA}$ prepared using a high Cu^{2+} precursor concentration (Section S1.4.1) acquired using the fluorescence (black trace) and TEY (blue trace) methods. (B) XAS data for a sample of **1**$_{BA}$ prepared using a low Cu^{2+} precursor concentration (Section S1.4.2) acquired using the fluorescence (black trace) and TEY (green trace) methods. In each case, both techniques give nearly identical results.
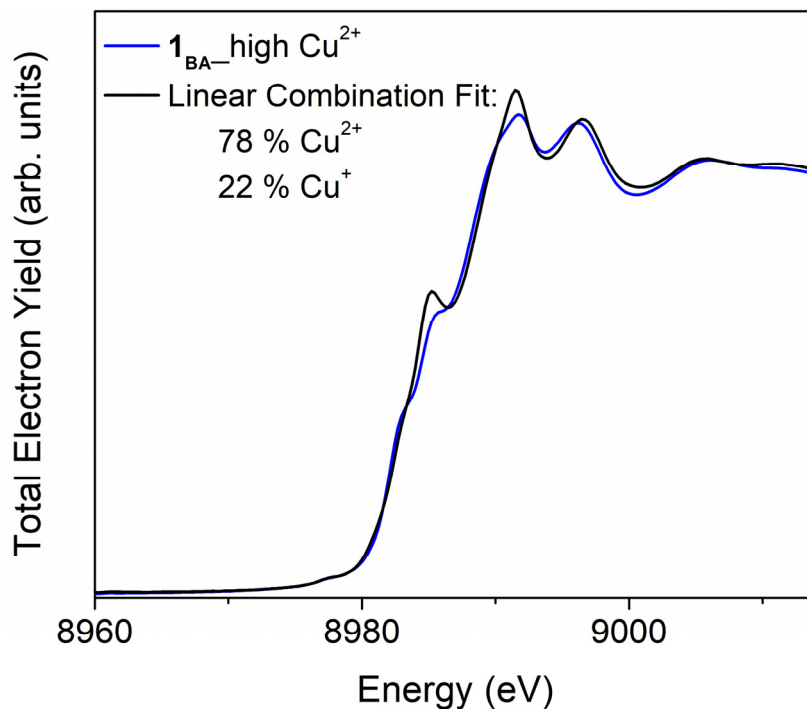

Figure S6 Linear combination fit of the TEY XAS data for a sample of **1**$_{BA}$ prepared using a high Cu^{2+} concentration (Section S1.4.1). The fit estimates the Cu^{2+}:Cu^+ ratio as 78:22.
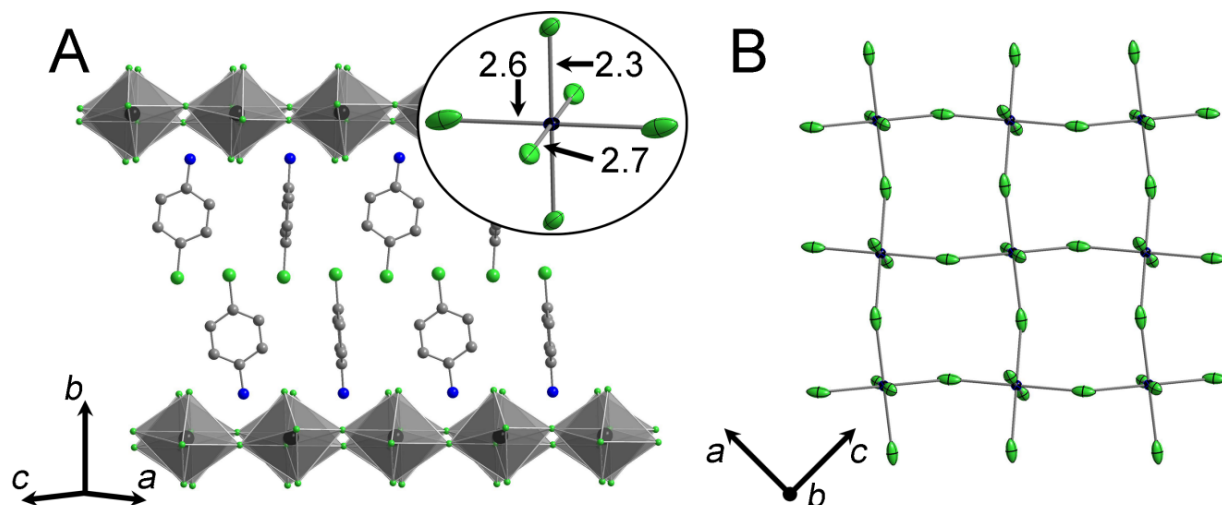
Figure S7 100 K SCXRD structure of **1$_{PCA}$** (A) with an inset showing the coordination environment about the B site. The elongation of the thermal ellipsoids of the equatorial Cl atoms is evident from the inset to A and from the top-down view of the perovskite lattice shown in B. Thermal ellipsoids are drawn at 50% probability. Green, gray and blue spheres represent Cl, C, and N atoms, respectively, while black spheres represent mixed Cu/In sites. H atoms omitted for clarity.
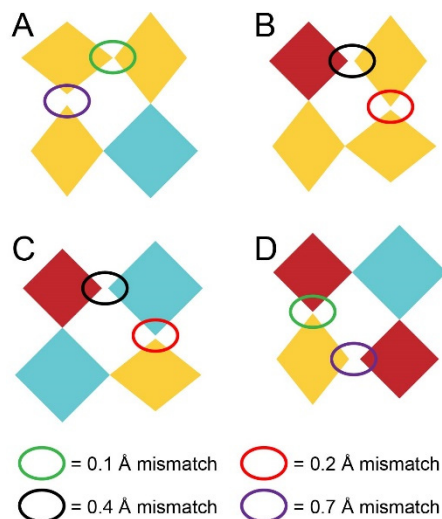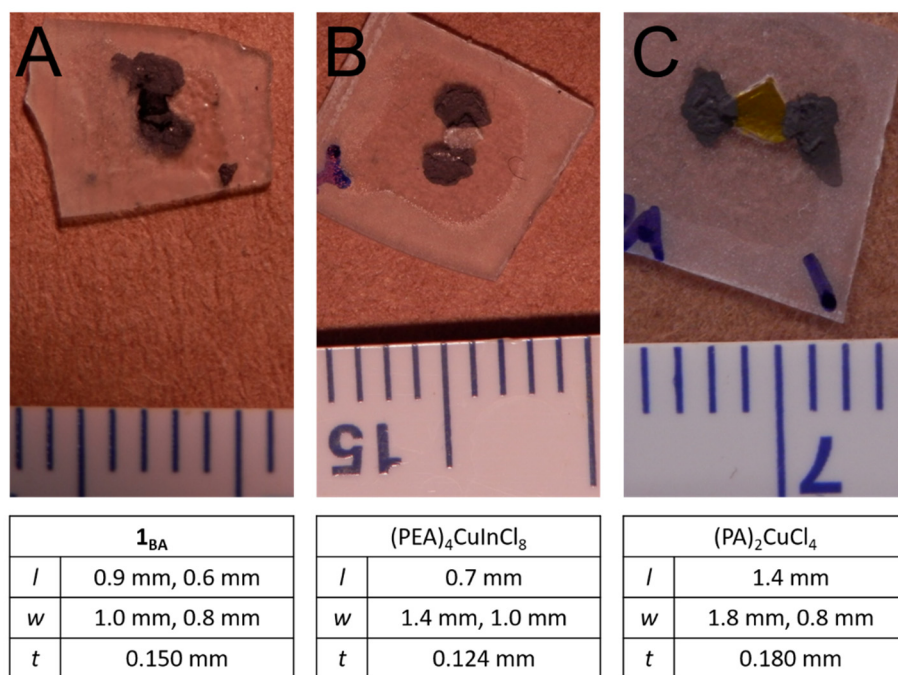

Figure S8 Clusters of $[In^{III}Cl_6]^{3-}$, $[Cu^{I}Cl_6]^{5-}$, and $[Cu^{II}Cl_6]^{4-}$ units that will become increasingly prevalent as the $Cu^{2+}:Cu^{+}:In^{3+}$ ratio deviates significantly from 2:1:1. Notably, these clusters have significantly greater packing mismatch than that in Figure S9A, as highlighted by the colored ovals which denote the severity of each mismatch site.
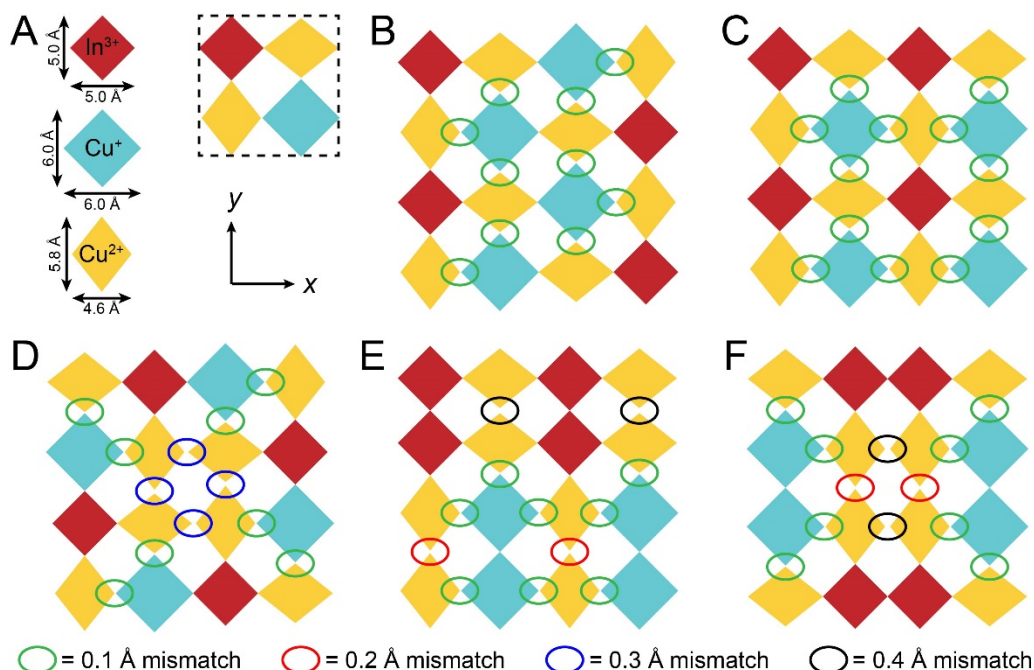
Figure S9 Top-down view of an $n = 1$ perovskite sheet showing various packing arrangements of $[In^{III}Cl_6]^{3-}$, $[Cu^{I}Cl_6]^{5-}$, and $[Cu^{II}Cl_6]^{4-}$ units (shown as red squares, blue squares, and yellow diamonds, respectively) with dimensions proportional to those found in the parent $(PEA)_4CuInCl_8$ and $(PCA)_2CuCl_4$ lattices (A). Two $[Cu^{II}Cl_6]^{4-}$ units, one $[Cu^{I}Cl_6]^{5-}$ unit, and one $[In^{III}Cl_6]^{3-}$ unit can be arranged into the cell shown in A. Translations of this unit along the x and y vectors accompanied by rotations or reflections generate the packing arrangements shown in B-F. Mismatches in the packing arrangements where corners of polyhedra do not come together exactly are marked with ovals where the color of the oval denotes the magnitude of the mismatch.
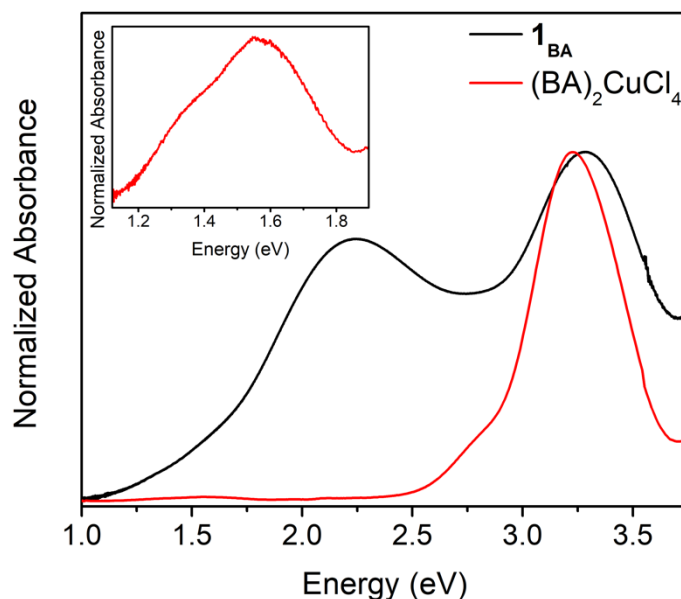

Figure S10 Thin-film transmission spectra of 1_{BA} (black trace) and $(BA)_2CuCl_4$ (red trace). The inset enlarges the weak absorption of the d-d transitions in $(BA)_2CuCl_4$.

1_BA	
l	0.9 mm, 0.6 mm
w	1.0 mm, 0.8 mm
t	0.150 mm

(PEA)$_4$CuInCl$_8$	
l	0.7 mm
w	1.4 mm, 1.0 mm
t	0.124 mm

(PA)$_2$CuCl$_4$	
l	1.4 mm
w	1.8 mm, 0.8 mm
t	0.180 mm

Figure S11 Examples of crystals of **1$_{BA}$** (A), (PEA)$_4$CuInCl$_8$ (B), and (PA)$_2$CuCl$_4$ (C) used for single-crystal conductivity measurements. Approximate crystal dimensions are shown below each picture. The length (distance between contacts, *l*) and width (*w*) of each sample was estimated using the scalebar while the thickness (*t*) was measured using a micrometer. Maximum and minimum values of *l* and *w* are given for cases where these values differed substantially.
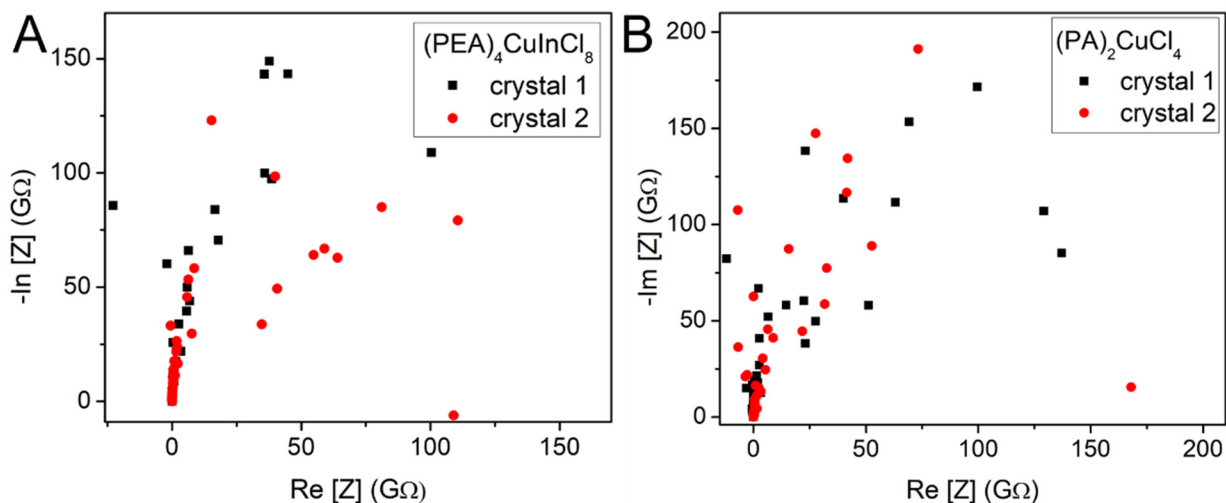

Figure S12 Nyquist plots for (PEA)$_4$CuInCl$_8$ (A) and (PA)$_2$CuCl$_4$ (B) at ambient temperature (ca. 28 °C) measured at an AC bias of 1 V. The data are highly scattered due to noise, demonstrating the highly insulating nature of these materials. No conductivity value could be extracted as a result.
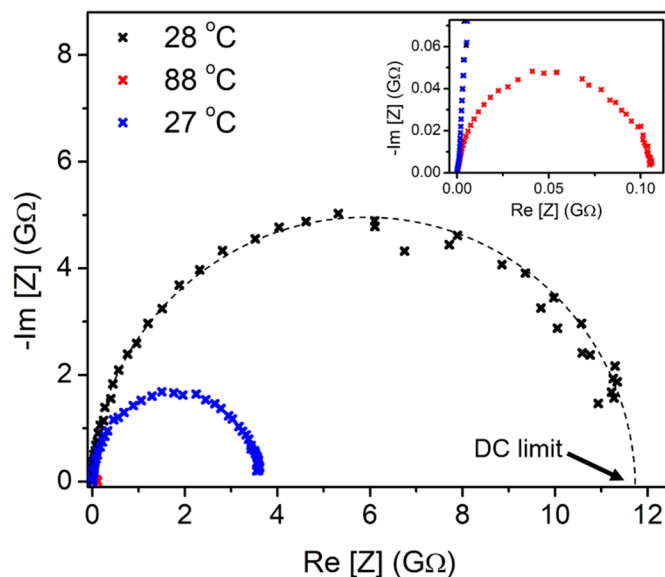
Figure S13 Nyquist plot for a crystal of **1**$_{BA}$ measured at 28 °C (black points). The black dotted line demonstrates how the data were extrapolated to approximate the resistance at the DC limit. After measuring the crystal at 28 °C, it was measured at a range of higher temperatures (see entries in Table S6 for crystal 1) ultimately reaching 88 °C (red points). The crystal was then returned to 27 °C and re-measured (blue points) exhibiting a ca. 3-fold higher conductivity than before heating.
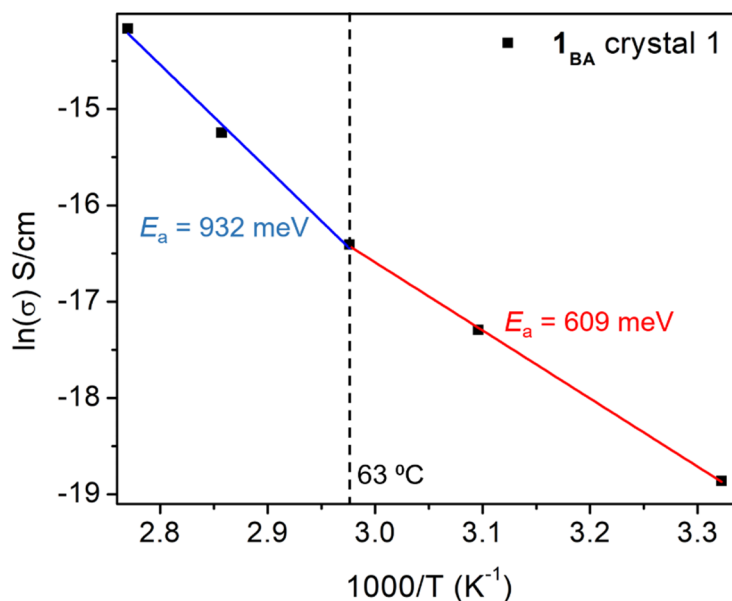

Figure S14 Plot of ln(σ) vs. 1000/*T* for crystal 1 of **1**$_{BA}$ with linear fits to the low and high temperature regions shown as red and blue lines, respectively. A significantly different slope is evident for the high temperature region, yielding a very different value of E_a (932 meV, R^2 = 0.990) than the lower temperature region (609 meV, R^2 = 0.999). For this reason, we use only the low temperature region to estimate E_a for this crystal (Section S2.9).
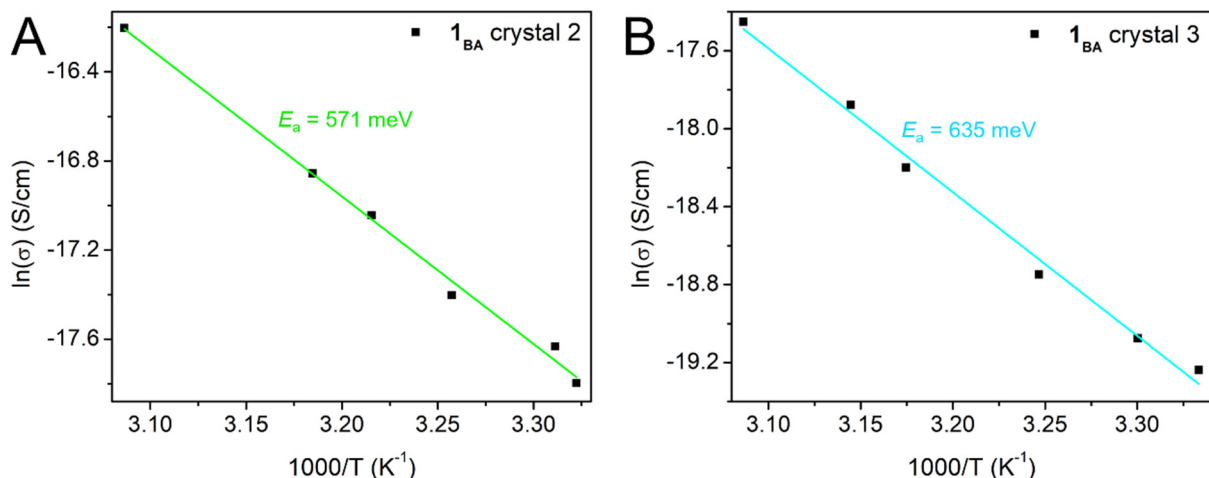
Figure S15 Plot of ln(σ) vs. 1000/*T* for (A) crystal 2 and (B) crystal 3 of **1$_{BA}$** (see Table S6 for σ and *T* values) with linear fits of the data shown as a green and blue lines, respectively. The slope of these lines yields E_a = 571 meV (R^2 = 0.991) for crystal 2 and E_a = 635 meV (R^2 = 0.993) for crystal 3.
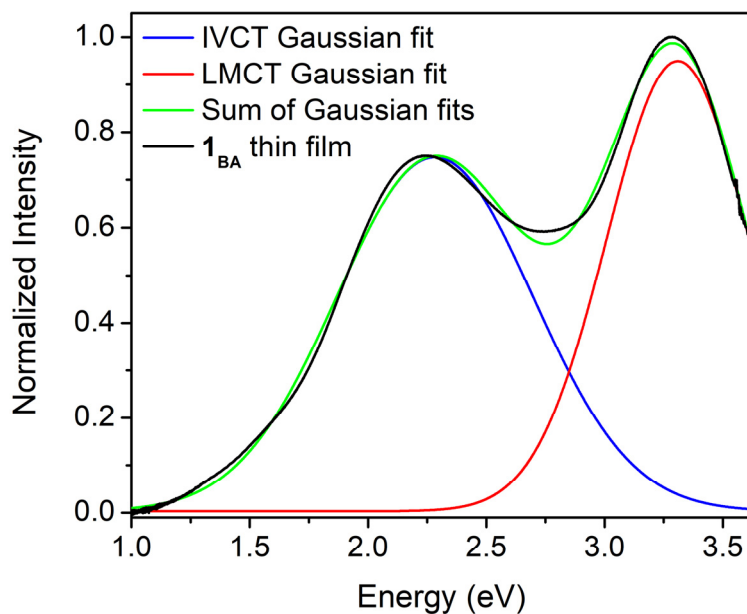

Figure S16 Thin-film transmission spectrum of **1$_{BA}$** (black trace) showing Gaussian fits (Equation S16) of the IVCT and LMCT features (blue and red traces, respectively). The green trace shows the sum of these Gaussian peaks and is a good match to the experimental spectrum. Fitting parameters for the two Gaussian peaks are given in Table S7.
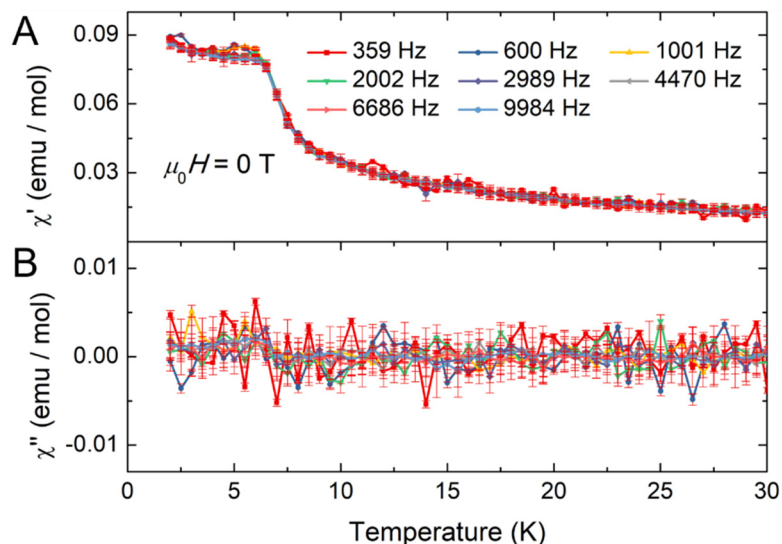
Figure S17 Frequency dependence of the (A) real (χ') and (B) imaginary (χ'') parts of the AC susceptibility, respectively, of crystals of **1$_{BA}$** measured in zero applied field. The data demonstrate the frequency-independence of the AC susceptibility of **1$_{BA}$** (though the lower-frequency data display a higher degree of noise than the higher-frequency data). Discrepancies in the low-temperature ($T < \sim 7$ K) behavior displayed here compared to the unoriented powder sample shown in the main text (Figure 6A, inset) likely arise from non-random orientation of the plate-like crystals, which display highly anisotropic magnetic behavior due to their layered crystal structure.
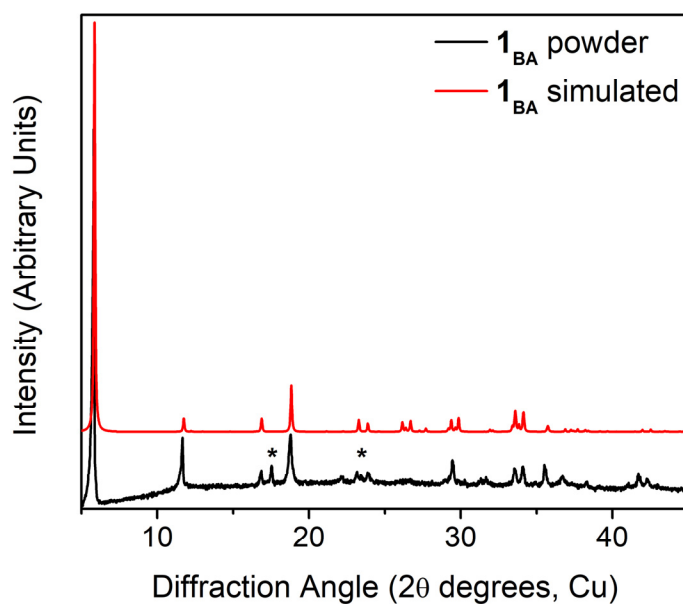

Figure S18 Powder XRD pattern of **1$_{BA}$** (black trace) and the pattern simulated from the room-temperature SCXRD data (red trace). The peaks marked with asterisks (*) correspond to the (003) and (004) reflections that are significantly more intense in the experimental spectrum than in the simulated spectrum. This may arise due to preferred orientation, which is difficult to eliminate even with thorough grinding due to the plate-like morphology of crystals of **1$_{BA}$**. It may also arise due to the poor SCXRD data quality for **1$_{BA}$** (Section S2.2) which could lead to inaccurate predictions of PXRD peak intensity.
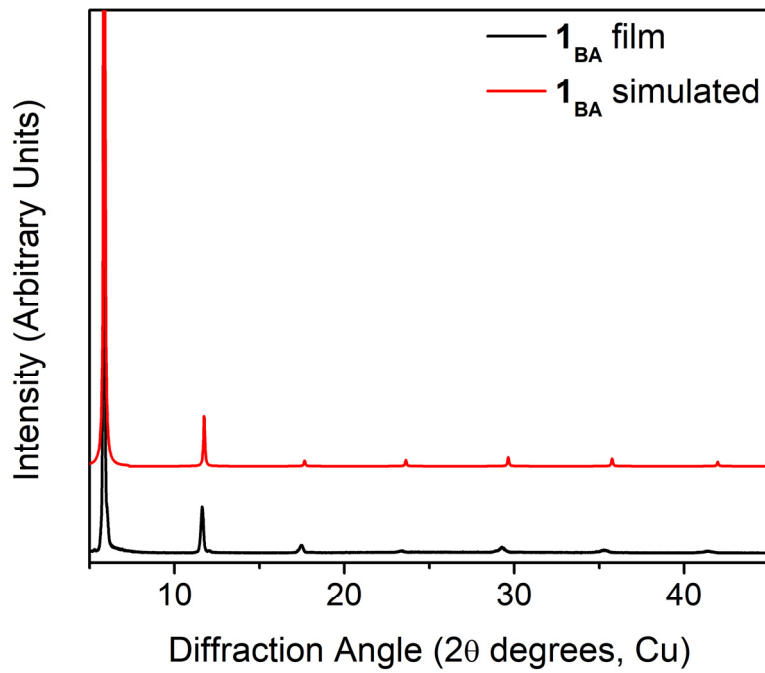
Figure S19 PXRD pattern of a thin film of **1$_{BA}$** (black trace) and the pattern simulated from the room-temperature single-crystal data assuming (001) preferred orientation (red trace).
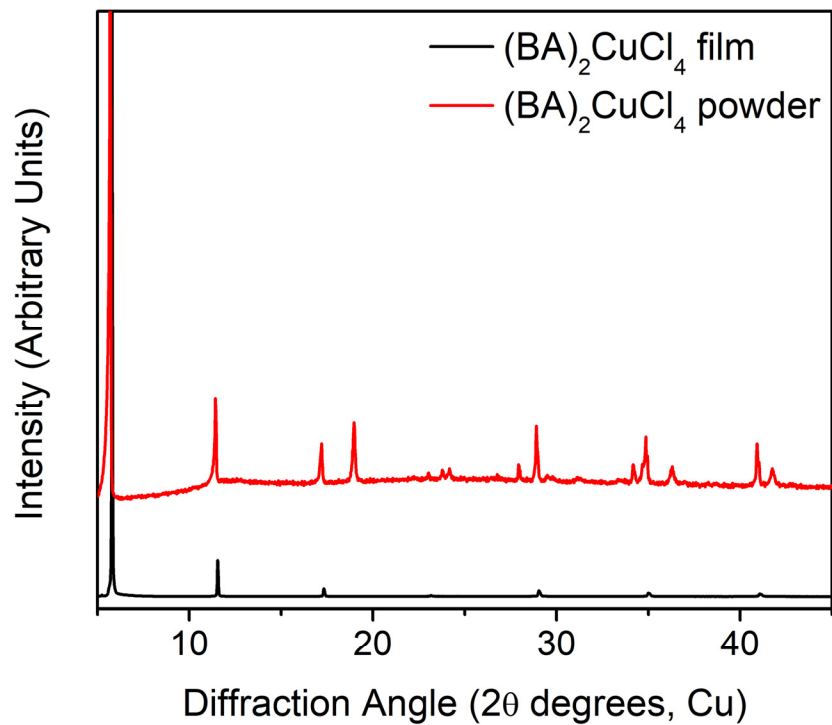
Figure S20 PXRD pattern of a finely ground powder (red trace) and a thin film (black trace) of (BA)$_2$CuCl$_4$ (red trace).
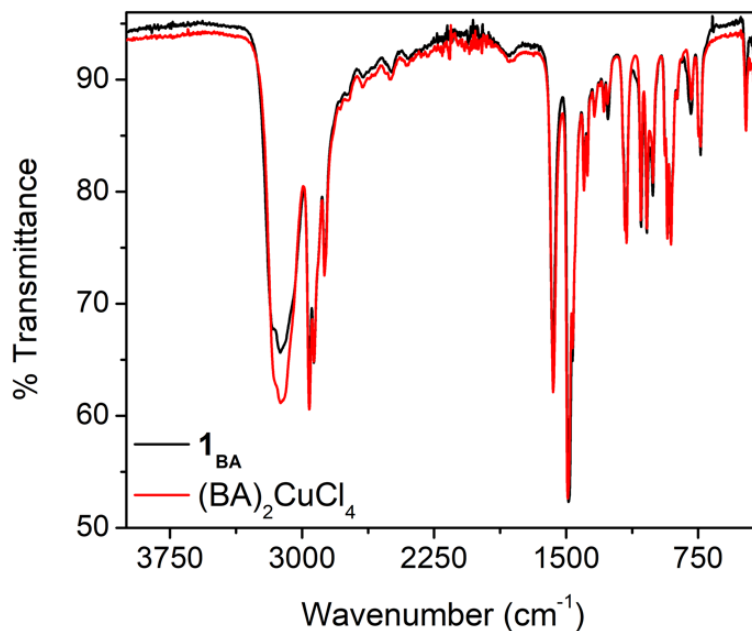
Figure S21 Infrared (IR) absorption spectrum of **1**$_{BA}$ (black trace) and $(BA)_2CuCl_4$ (red trace) demonstrating the near identicality of these two spectra.

S4 References

(1) Jaffe, A.; Karunadasa, H. I., Lithium Cycling in a Self-Assembled Copper Chloride−Polyether Hybrid Electrode. *Inorg. Chem.* **2014**, *53*, 6494-6496.

(2) *SAINT and SADABS*, Bruker AXS Inc.: Madison, Wisconsin, 2007.

(3) Sheldrick, G. M. *SHELXL-97, A program for crystal structure refinement*; Göttingen: 1997.

(4) Sheldrick, G. M., A short history of *SHELX. Acta Crystallogr., Sect. A: Found. Crystallogr.* **2008**, *64*, 112-122.

(5) Dolomanov, O. V.; Bourhis, L. J.; Gildea, R. J.; Howard, J. A. K.; Puschmann, H., *OLEX2*: a complete structure solution, refinement and analysis program. *J. Appl. Crystallogr.* **2009**, *42*, 339-341.

(6) Müller, P.; Herbst-Irmer, R.; Spek, A. L.; Schneider, T. R.; Sawaya, M. R., *Crystal Structure Refinement: A Crystallographer's Guide to SHELXL*. Oxford University Press: New York, 2006.

(7) Ravel, B.; Newville, M., ATHENA, ARTEMIS, HEPHAESTUS: data analysis for X-ray absorption spectroscopy using IFEFFIT. *J. Synchrotron Radiat.* **2005**, *12*, 537-541.

(8) Slavney, A. H.; Leppert, L.; Saldivar Valdes, A.; Bartesaghi, D.; Savenije, T. J.; Neaton, J. B.; Karunadasa, H. I., Small-Band-Gap Halide Double Perovskites. *Angew. Chem. Int. Ed.* **2018**, *57*, 12765-12770.

(9) McClure, E. T.; McCormick, A. P.; Woodward, P. M., Four Lead-free Layered Double Perovskites with the *n* = 1 Ruddlesden–Popper Structure. *Inorg. Chem.* **2020**, *59*, 6010-6017.

(10) Bi, L.-Y.; Hu, T.-L.; Li, M.-Q.; Ling, B.-K.; Lassoued, M. S.; Hu, Y.-Q.; Wu, Z.; Zhou, G.; Zheng, Y.-Z., Template effects in Cu(I)-Bi(III) iodide double perovskites: a study of crystal structure, film orientation, band gap and photocurrent response. *J. Mater. Chem. A* **2020**, *8*, 7288-7296.

(11) Connor, B. A.; Leppert, L.; Smith, M. D.; Neaton, J. B.; Karunadasa, H. I., Layered Halide Double Perovskites: Dimensional Reduction of $Cs_2AgBiBr_6$. *J. Am. Chem. Soc.* **2018**, *140*, 5235-5240.

(12) Elliott, N.; Pauling, L., The Crystal Structure of Cesium Aurous Auric Chloride, $Cs_2AuAuCl_6$, and Cesium Argentous Auric Chloride, $Cs_2AgAuCl_6$. *J. Am. Chem. Soc.* **1938**, *60*, 1846-1851.

(13) Castro-Castro, L. M.; Guloy, A. M., Organic-Based Layered Perovskites of Mixed-Valent Gold(I)/Gold(III) Iodides. *Angew. Chem., Int. Ed.* **2003**, *42*, 2771-2774.

(14) Schröder, L.; Keller, H.-L., Darstellung und Kristallstruktur von $Cs_2HgPdCl_6$, eine Verzerrungsvariante der Chloroperowskite. *Z. Anorg. Allg. Chem.* **1991**, *603*, 69-76.

(15) Aubrey, M. L.; Saldivar Valdes, A.; Connor, B. A.; Filip, M. R.; Neaton, J. B.; Karunadasa, H. I., Directed assembly of layered halide perovskite heterostructures. *In Review*.

(16) Eaton, G. R.; Eaton, S. S.; Barr, D. P.; Weber, R. T., *Quantitative EPR: A Practitioners Guide*. Springer-Verlag: Vienna, 2010.

(17) Mazur, M., A dozen useful tips on how to minimise the influence of sources of error in quantitative electron paramagnetic resonance (EPR) spectroscopy—A review. *Anal. Chim. Acta* **2006**, *561*, 1-15.

(18) Connor, B. A.; Biega, R.-I.; Leppert, L.; Karunadasa, H. I., Dimensional reduction of the small-bandgap double perovskite $Cs_2AgTlBr_6$. *Chem. Sci.* **2020**, *11*, 7708-7715.